applied sciences

MDPI

Article

A New Approach to the Study of Multi-Pass Welds–Microstructure and Properties of Welded 20-mm-Thick Superduplex Stainless Steel

Maria Asuncion Valiente Bermejo [1,*], Kjell Hurtig [1], Daniel Eyzop [2] and Leif Karlsson [1]

[1] Department of Engineering Science, University West, 461 32 Trollhättan, Sweden; kjell.hurtig@hv.se (K.H.); leif.karlsson@hv.se (L.K.)

[2] Outokumpu Stainless AB, Avesta R&D Center, 774 41 Avesta, Sweden; daniel.eyzop@outokumpu.com

* Correspondence: asun.valiente@hv.se

Received: 12 February 2019; Accepted: 11 March 2019; Published: 13 March 2019

Abstract: Type 2507 superduplex stainless steel 20 mm in thickness was multi-pass-welded with Gas Metal Arc Welding (GMAW) and Flux-Cored Arc Welding (FCAW) processes. Recommended and higher arc energies and inter-pass temperatures were used. Thermal cycles were monitored using a recently developed procedure involving the successive instrumentation of the multi-pass welds, pass by pass, by addition of thermocouples in each weld pass. The repeatability of temperature measurements and survival rate of more than 90% of thermocouples confirmed the reliability of the procedure. Reheating by subsequent passes caused a progressive increase in the austenite content of the weld metal. The as-deposited GMAW passes with higher-than-recommended arc energy showed the lowest presence of nitrides. Therefore, the cooling rate—and not the time exposed at the critical temperature range—seems to be the key factor for nitride formation. The welding sequence layout also plays an important role in the distribution of secondary phases. A larger amount and concentration of secondary austenite and σ-phase was found for a larger number of subsequent passes in the immediate vicinity of a specific weld pass. The impact toughness exceeded requirements for all welds. Differences in absorbed energies were related to the amount of micro-inclusions found with the FCAW weld showing the lowest absorbed energies and highest amount of micro-inclusions. Pitting corrosion preferentially initiated in locations with secondary austenite and σ-phase. However, in the absence of these secondary phases, the HAZ containing nitrides was the weakest location where pitting initiated. The results of this work have implications on practical welding for superduplex stainless steels: the current recommendations on maximum arc energy should be revised for large thickness weldments, and the importance of the welding sequence layout on the formation of secondary phases should be considered.

Keywords: welding; superduplex stainless steel; multi-pass welding; thermal cycles; secondary austenite; σ-phase; nitrides

1. Introduction

Since the beginning of the 1990s duplex and superduplex stainless steels have played an essential role in the oil and gas industry, in transportation, in construction applications, and in the process industry [1].

However, the practical application of superduplex stainless steels using large thickness plates and pipes is strongly dependent on the use of welding for fabrication, and there is still an important lack of knowledge regarding multi-pass welding of these steels. In multi-pass welding, some areas of the weld region are repeatedly heated. It is well known that when heated to, and in particular

when repeatedly heated to, the range of approximately 600 to 1000 °C, superduplex stainless steels and weld metals are prone to intermetallic phase formation (e.g., σ-phase, χ-phase, and R-phase) [2,3]. Reheating can also induce secondary austenite formation and nitride precipitation. The presence of these phases is strongly detrimental to corrosion resistance and toughness.

Measuring and monitoring temperatures is a key stage in quality control and process productivity for multiple industrial processes, including welding. However, measuring temperatures during welding shows experimental difficulties caused by the welding process itself. Welding fumes, sparks, or light reflections can be important sources of error when using non-contact techniques for temperature measurements. Alternatively, the use of contact techniques such as thermocouples also presents difficulties: the electric arc can interfere with the signal, and the high power beams can burn the thermocouples. It might also happen that some displacement in the location of the thermocouples occurs because of the motion and flow in the weld pool, causing therefore uncertainty in the positioning of the final measurement location. Several previous studies have focused on temperature measurements, i.e., in laser welding of austenitic stainless steels [4,5], in Gas Tungsten Arc Welding (GTAW) of duplex stainless steels [6,7], and in laser metal deposition of nickel alloys [8]. The involvement of the current paper's authors in the previously cited research was a helpful background to develop and establish the method used in this research to measure and monitor temperatures during multi-pass welding.

This work aimed at making multi-pass welding of large thickness superduplex stainless steels more efficient by investigating the influence of the multiple welding cycles on the formation of undesirable phases. Therefore, the recently developed method for monitoring local thermal cycles was applied in GMAW and FCAW multi-pass welding of 20-mm-thick superduplex stainless steel. The thermal cycles were correlated to the local microstructure and to impact toughness and corrosion resistance. The findings in this research have some implications on the current practical welding guidelines, suggesting a review in case of large thickness weldments.

2. Materials and Methods

2.1. Materials and Welding Experiments

Type 2507 superduplex stainless steel (EN 1.4410, UNS S32750) plates 20 mm in thickness were welded with mechanized GMAW and FCAW. For FCAW, the arc energy and interpass temperature were according to those recommended by guidelines and practices [9–11] (experiment FR). However, for GMAW, two approaches were tried, one with the recommended interpass temperature and arc energy (experiment GR) and another with higher-than-recommended interpass temperature and arc energy (experiment GH). Table 1 summarizes the experiments and main settings, and Figure 1 shows the welds layout. Table 2 includes the designation and chemical composition of the base and filler materials. All filler materials used were ø 1.2 mm, and the backing gas in all the experiments was N2 gas (>99.95% purity), applied during welding of the root.

The selection of the shielding gas for GMAW welding was initially based on previous research [12,13]. However, a recent study [14] and preliminary trials in this project confirmed that small amounts of arc stabilizing components (O_2, CO_2) in the shielding gas caused porosity in superduplex multi-pass welds with more than 3 passes. Therefore, the shielding gas selected for GMAW was Ar + 30%He. For FCAW, MISON 18 was used, as this is the recommended gas for this consumable; for the GTAW root in the GR experiment, the shielding gas was MISON N2.

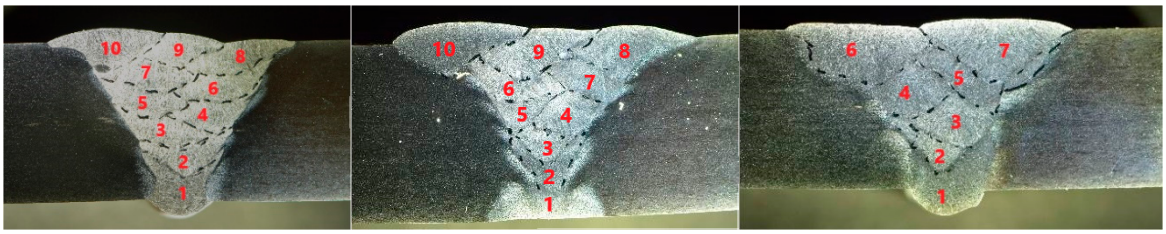

Figure 1. Welding sequence layout. (**Left**) FR weld; (**Center**) GR weld; (**Right**) GH weld.

Table 1. Experimental settings.

Ref.	Welding Process	Arc Energy (kJ/mm)		Recorded Inter-Pass Temperature (°C)	Joint Prep.	Number of Weld Passes
		Root Pass (p1)	Pass 2 to Last Pass			
GR	GMAW	1.5	1.2–1.3	80–100	V with GTAW root	10
FR	FCAW	1.5	1.1–1.3	80–100	V with ceramic backing	10
GH	GMAW	2.0	2.2	174–196	V with ceramic backing	7

Table 2. Designation and chemical composition of the plate and the fillers. For GTAW and GMAW, it refers to the wire composition, whilst for FCAW it refers to the all-weld composition (wt %).

Designation	C	Si	Mn	P	S	Cr	Ni	Mo	Cu	N	W
20 mm plate EN 1.4410, UNS S32750	0.012	0.38	0.76	0.023	0.001	25.1	6.91	3.82	0.22	0.29	-
GTAW: AWS SFA5.9 ER2594	0.013	0.46	0.65	0.016	0.001	25.16	9.25	3.91	0.09	0.270	0.01
GMAW: AWS SFA5.9 ER2594	0.015	0.40	0.61	0.014	0.001	25.23	9.22	4.04	0.09	0.260	0.04
FCAW: AWS SFA5.22 E2594T1-4/-1	0.026	0.66	1.07	0.023	0.004	25.81	9.57	3.70	0.09	0.230	0.01

2.2. Methodology to Study Multi-Pass Welds

The base material plates were V-60 bevelled and tacked along the 500 mm edge to be welded. The root pass filled the complete groove length (500 mm), but every subsequent weld pass was shortened 50–70 mm in length from the previous weld pass length, as shown in Figure 2. The aim was to have one coupon containing the last (as-deposited) pass and the previous ones. Therefore, it was possible to obtain, for each weld pass, a section to characterize the weld and HAZ microstructure and to follow the evolution of the microstructure after each thermal cycle experienced by the material.

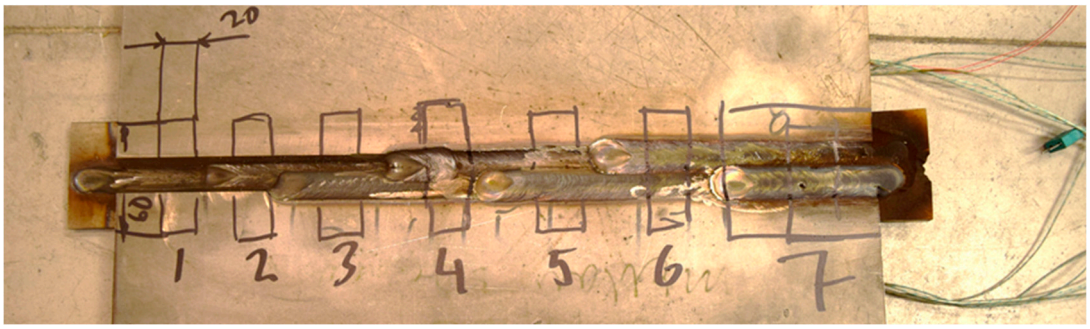

Figure 2. Welding configuration used to extract coupons to study the evolution of the microstructure caused by the subsequent weld passes. The numbers from 1 to 7 correspond to the locations where coupons with passes from 1 to 7 were extracted and contained that number of weld passes, i.e., 1 means one weld pass, 2 means two weld passes, and so forth until 7, including the seven weld passes in the GH weldment.

The microstructural inspection included the evaluation of the general microstructure and the presence of secondary phases: nitrides, secondary austenite (γ_2), and σ-phase in the weld metal and the HAZ.

The measurement and recording of the temperatures was conducted by successive instrumentation of the multi-pass welds, pass by pass, by addition of thermocouples in each weld

pass. A combination of K-type thermocouples, (1) harpooned in the melt pool and (2) inserted from the backside through 2 mm drilled holes from previously deposited passes and spot welded on the surface of the joint, was used. Figure 3 shows two inserted thermocouples after drilling—the plate and previous weld passes—and spot welding them to the surface of the joint. Figure 4 illustrates the layout of the inserted thermocouples at the back side of the joint and the harpooned thermocouples at the top side of the joint. At each weld pass, 2–4 thermocouples were added to record the thermal cycles. Up to 32 thermocouples were used to record the thermal cycles simultaneously in one weld.

Figure 3. Example of two inserted thermocouples to register temperatures in Weld Pass 2. Holes of 2 mm in diameter were used to insert the thermocouples from the backside by drilling through the root pass. After the insertion, the thermocouples were spot welded on the surface of the joint—in this case, the surface of the root pass.

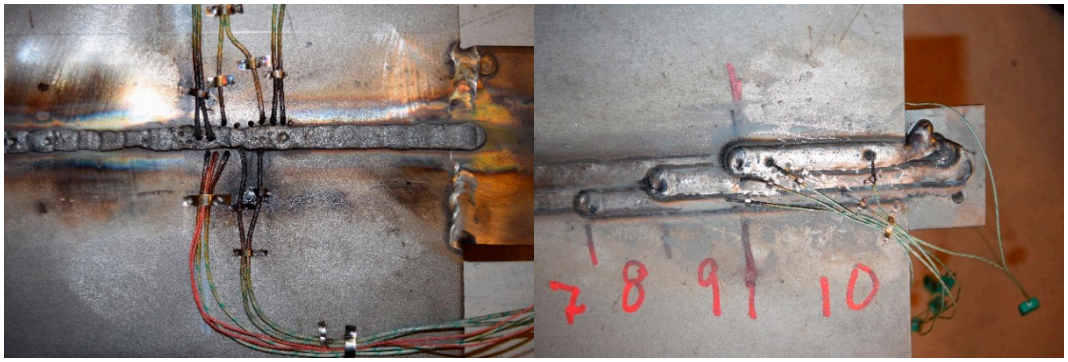

Figure 4. (**Left**) Back side of the joint showing the layout of the thermocouples inserted through drilled holes. (**Right**) Front side of the joint showing the layout of the harpooned thermocouples in the last passes. Note that the image shows the harpooned thermocouples only in the last passes because most of them have to be removed prior to welding of the following weld pass.

2.3. Equipment and Testing

Ferrite content in the weld metal was measured by the magnetic permeability technique (Fischer Feritscope FMP30). It has to be noted that ferrite content measured by magnetic permeability was converted to and displayed as % ferrite by Fischer Feritscope's internal correlation. The reason for this was to present ferrite content using the same unit as in the image analysis evaluation done for the HAZ, although this is not included in the current paper. Light optical microscopy (Olympus BX60M, Zeiss AxioCam MRC5) was used for microstructural characterization and image analysis. Electrolytic

etching with 40% NaOH was selected to reveal the general microstructure and σ-phase, whilst 10% oxalic acid was used to reveal nitrides.

Impact toughness testing was conducted in the weld metal and the HAZ according to ISO 9016 [15]. A total of 36 specimens were tested, 12 per experiment, which corresponds to three repetitions for each temperature and location.

Corrosion testing was performed following ASTM G48E [16] for a total of 30 coupons, 10 per experiment, to evaluate the critical pitting temperature (CPT). This test is normally considered for surfaces in contact with the media, not for cross sections. However, in this study, the cross section was the area of interest. In such large size specimens, it was decided not to consider the weight loss criterion established by Norsok M-601 (<4 g/m^2) because the results might not reflect the true corrosion resistance of the area. Instead, the criterion to pass the test was the absence of pits deeper than or equal to 0.025 mm.

To compare the influence of the arc energy on the pitting corrosion resistance of the GMAW welds, the ASTM G150 test [17] was performed on coupons extracted 6 mm from the root. The test was stopped as soon as 0.1 mA/cm^2 was registered in order to find the most susceptible location to pitting corrosion. Since the 60 s holding time requested by the standard was not kept after registering the 0.1 mA/cm^2, the temperature at which pitting started was not strictly speaking the CPT, but it served for comparison purposes.

Finally, weld metal oxygen content was analyzed in a LECO TC-436 furnace.

2.4. Evaluation of Thermal Cycles

The recorded thermal cycles were used for different purposes. Firstly, the cooling rates based on the cooling times between 1200 and 800 °C ($t_{12/8}$) were calculated. Secondly, the time that each weld run was exposed to critical temperature ranges for the formation of secondary phases was calculated.

In the selection of critical temperature ranges for the formation of secondary phases, data available in the literature and extracted from computational thermodynamics (JMatPro, Sente Software, Surrey, UK) were used. For intragranular secondary austenite (γ_2), formation was assumed to happen at temperatures higher than 500 °C [2,18] and dissolution at temperatures around 1375 °C [19]. For chromium nitrides, the temperature range for most rapid formation was from 700 to 900 °C [2] and dissolution around 1070 °C according to JMatPro. The upper temperature for σ-phase formation was calculated based on the experimental chemical composition of the welds using JMatPro. The lower temperature for relatively rapid formation was set to 750 °C as TTT diagrams by JMatPro showed that around 100 s at that temperature would be required to have 0.1% σ-phase precipitated. The upper temperature was found to be between 1055 and 1073 °C, depending on the specific weld metal composition considered. A temperature of 1073 °C was selected to be the upper temperature for σ-phase in the analysis of the thermal cycles.

The following approach was used to calculate the time that each weld run was exposed to critical temperature ranges in the formation of secondary phases: In those weld passes where the liquidus temperature was reached, only the cooling part of the thermal cycle curve was considered. However, in the weld passes where the liquidus temperature was not reached, the heating and cooling branches of the thermal cycle were considered. The thermal cycles were also used to evaluate a possible dissolution of nitrides and σ-phase at temperatures above their upper temperature for thermodynamic stability; hence by calculating the time at which the weld passes were exposed at temperatures higher than those upper temperatures.

3. Results

In this chapter, two different types of results are presented: firstly, results related to the reliability of the methodology used for the temperature measurements and, secondly, results in connection to the microstructure and properties of the multi-pass welds.

3.1. Reliability of Temperature Measurements

Using a combination of K-type thermocouples, which were (1) harpooned in the melt pool and (2) inserted from the backside through 2 mm drilled holes from previously deposited passes and spot welded on the surface of the joint, was successful, and more than 90% of thermocouples survived. When comparing the measurements obtained by the harpooned and the inserted thermocouples, very low dispersion (from 0.1 to 2.2 s) was found in the time at which the weld metal was exposed to the different temperature ranges of interest. As an example, the temperature vs. time registered during the welding of Weld Pass 7 in the GR weld is shown in Figure 5. Two thermocouples (tc 13 and tc 14) were inserted through drilled holes, whilst two other thermocouples (tc 15 and tc 16) were harpooned. The time at which Weld Pass 7 was exposed to the critical temperature ranges is also shown in Figure 5.

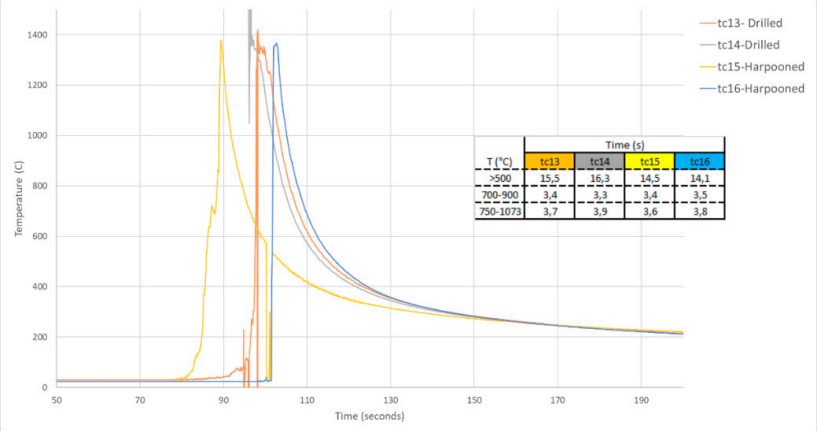

Figure 5. Temperature vs. time plots in Weld Pass 7 in the GR weld registered by using two thermocouples harpooned in the weld metal and two thermocouples inserted into drilled holes. The table embedded in the plot shows the time at which the deposited weld metal was exposed at the three ranges of temperatures studied.

To prove the accuracy of the temperatures measured by the thermocouples, the FR weld was placed in a furnace with the 20 thermocouples used to monitor the temperature in the weld passes connected (see Figure 6). All the thermocouples yielded a signal and reacted to the heat pulses in the furnace. Most importantly, the measurements obtained in the furnace proved to be accurate, with a range of dispersion of only 2 °C.

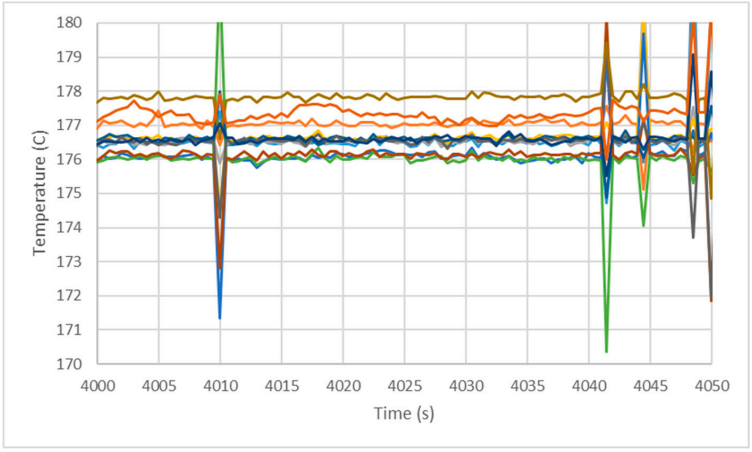

Figure 6. Temperature vs. time plot given by the thermocouples used in the FR weld inserted in a furnace. All the thermocouples yielded signal and reacted to the heat pulses in the furnace. Most importantly, the measurements proved to be accurate, within a range of dispersion of 2 °C.

3.2. Cooling Rates

The cooling rates were calculated based on the cooling time ($t_{12/8}$) registered by the thermocouples in the weld passes. Figure 7 shows the average cooling rate for the weld passes prepared with the same arc energy (Table 1). It was observed that the cooling rate increased with the number of welding passes and that the welding procedure with higher-than-recommended arc energy (GH) showed the lowest cooling rates.

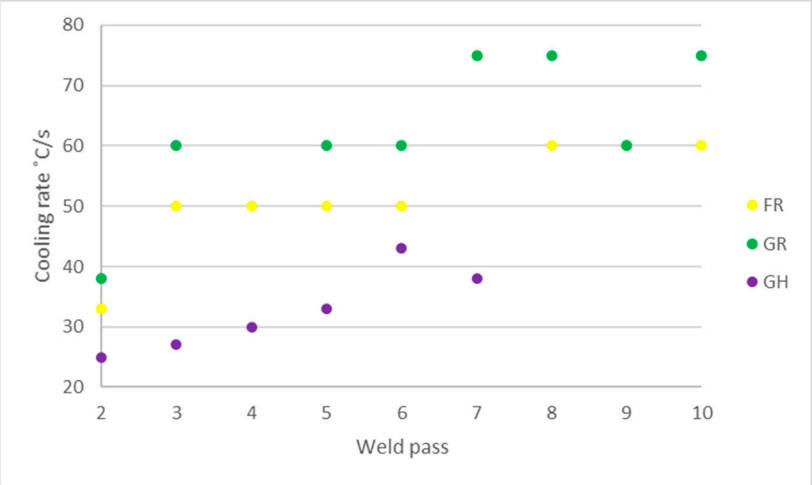

Figure 7. Average cooling rate between 1200 and 800 °C vs. weld pass number and welding procedure. Data for GR weld in Weld Pass 4 is not available because of a failure in the software that monitored the temperatures. The GH weld had only seven weld passes, which is why there are no data for Weld Passes 8, 9, and 10. Weld Pass 7 for FR and GR welds had exactly the same cooling rate (75 °C/s), which is why only one point is shown.

3.3. Phase Balance

In this work, the ferrite content was measured by magnetic permeability, pass by pass, so that the influence of the reheating on the ferrite content could be evaluated. Figure 8 presents the evolution in ferrite content of each weld pass for the three experiments. In 25% Cr superduplex stainless steels weldments, Norsok standard M-601 [20] requires a ferrite content between 30 and 70%. Ferrite in the weld passes for the three experiments was within the range established by Norsok M-601. The trend observed was a reduction in ferrite content and therefore an increase of austenite in the weld metal.

The ferrite content in the as-deposited condition and after the last reheating cycle were compared in Weld Pass 1 (the pass experiencing the largest number of reheating cycles). The GH weld showed the highest decrease with 12% ferrite reduction, the FR weld showed a decrease of 7% ferrite, and the GR weld showed a 4% ferrite reduction. The progressive increase in austenite content of the weld metal caused by subsequent reheating was confirmed by metallographic inspection (Figure 9). New austenite was formed: in the intragranular zones with the formation of secondary austenite, with the growth of the Widmanstätten austenite laths and with the growth of intergranular austenite.

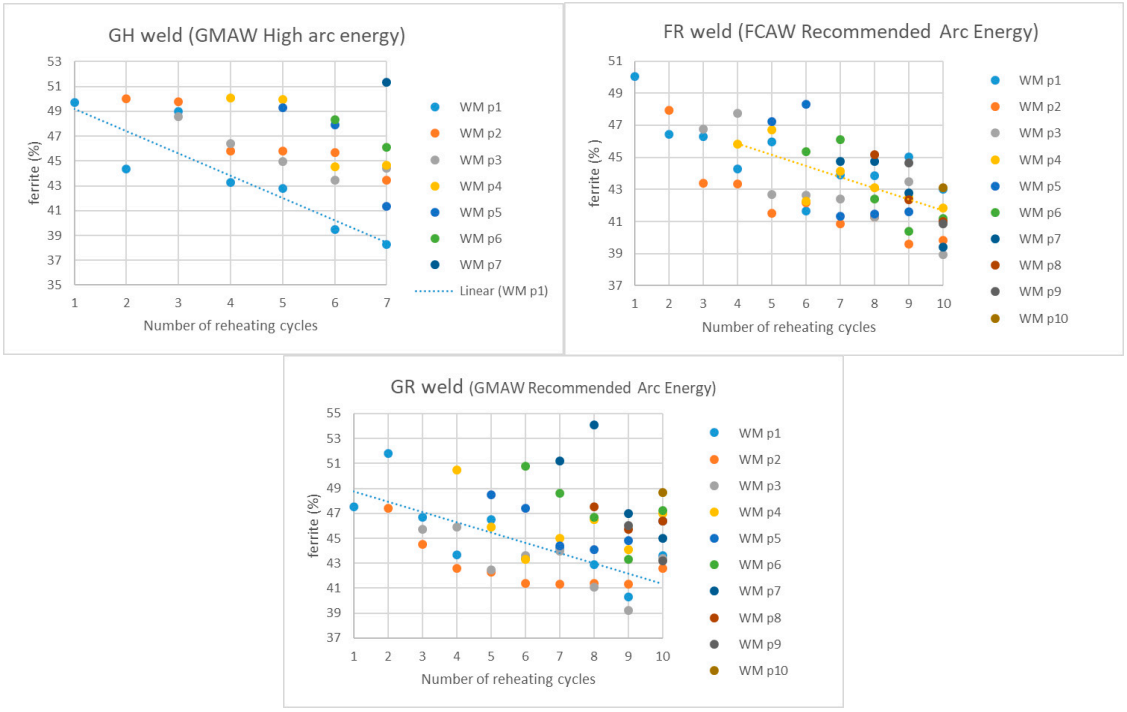

Figure 8. Ferrite content (Y-axis) measured by magnetic permeability pass by pass to evaluate the influence of the successive reheating on the ferrite content. A progressive reduction in ferrite content was observed in the weld metal. For better clarity of the reduction in ferrite, dotted lines show a linear regression of ferrite content in specific weld metal passes (Weld Pass 1 in the GH and GR welds and Weld Pass 4 in the FR weld). "WM pX" means the weld metal deposited in Weld Pass X.

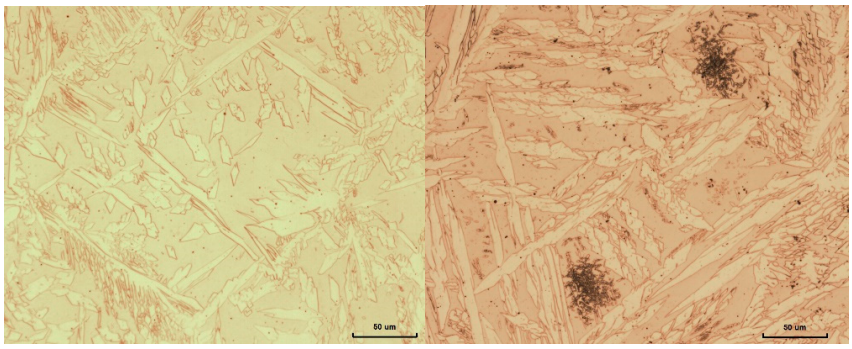

Figure 9. Micrographs of Weld Pass 1 in the GH weld. (**Left**) As-deposited. It shows Widmanstätten austenite laths within the ferritic matrix. (**Right**) After six reheating cycles. Widmanstätten austenite laths grew (an average of 4 μm thicker) and secondary austenite (small needle-shaped) was formed in the intragranular areas of the ferritic matrix.

3.4. Secondary Phases

The as-deposited GMAW passes with higher-than-recommended arc energy (GH) showed the lowest presence of nitrides and no nitrides in some cases, despite having remained longer times at the critical temperature ranges. The as-deposited GMAW passes with recommended arc energy (GR) showed the highest presence of nitrides and the FCAW with recommended arc energy was in between.

The root pass (GTAW) in the GR weld contained significant amounts of nitrides after only 6 s in the critical temperature range (Figure 10; Left). By far this pass showed most nitrides in the as-deposited pass compared to any other experiment. The first pass in the FR and GH welds presented a nitride-free microstructure despite the fact that they experienced longer times in the critical range. The cooling rate (based on the cooling time $t_{12/8}$) of the root GTAW pass was the same as the cooling rate of the

second GMAW weld pass (38 °C/s), which did not present nitrides (Figure 10; Right). However, the average size of the ferrite grains in the second GMAW weld was 87 μm +/−12 μm, whilst in the root GTAW pass it was 147 μm +/−35 μm.

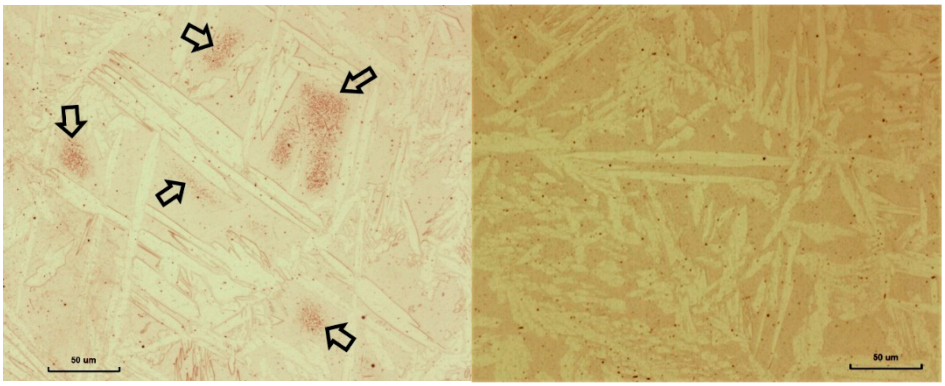

Figure 10. Influence of the grain size on the nitrides precipitation. First and second passes in GR weld cooled at the same cooling rate (38 °C/s). (**Left**) Root pass (GTAW) showing significant amounts of nitrides after only 6 s in the critical temperature range. Average ferrite grain size was 147 μm. (**Right**) Second pass (GMAW) not presenting nitrides after 6 s in the critical temperature range. Average ferrite grain size was 87 μm.

Regarding the HAZ, nitrides were found in the HAZ of all the passes. In the low-temperature heat-affected zone (LTHAZ), they were concentrated at a distance from the intergranular austenite, but also along the primary ferrite grain boundaries and in the δ/ɣ boundaries (Figure 11). The largest LTHAZ was found in the GTAW pass (root pass) of the GR weld, with nitrides found up to 2 mm from the fusion line. In the high-temperature heat-affected zone (HTHAZ), nitrides were mainly seen in the ferrite. Secondary austenite was only found in the reheated HTHAZ of the GH weld produced with higher-than-recommended arc energy. In that case, the secondary austenite was found in the former nitride locations (Figure 12).

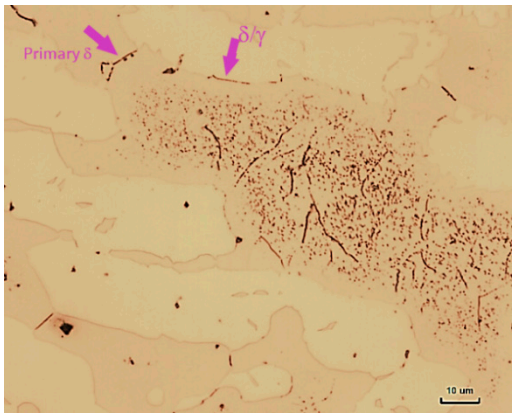

Figure 11. Preferential locations for precipitation of nitrides in the HAZ: primary ferrite grain boundaries, δ/ɣ boundaries and in the ferrite grains.

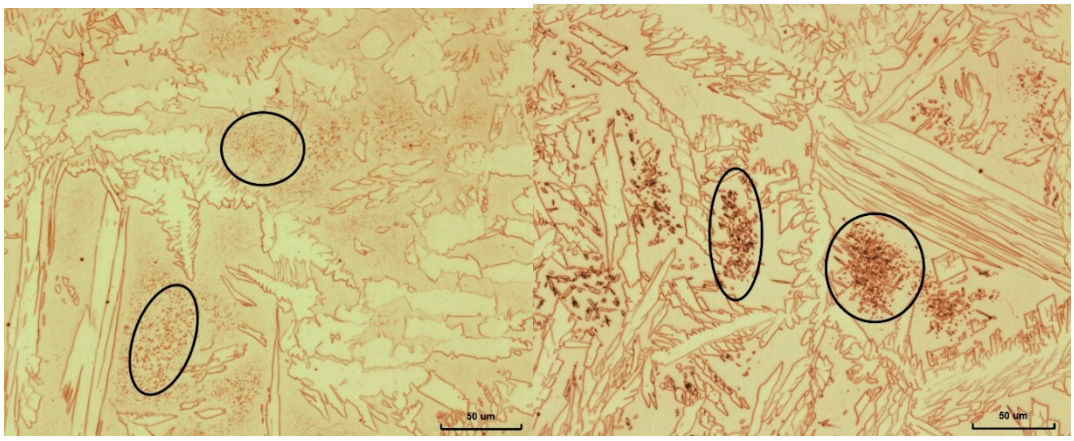

Figure 12. (**Left**) HTHAZ of Weld Pass 1 of the GH weld showing nitrides. (**Right**) HTHAZ of Weld Pass 1 of the GH weld after depositing two passes. Secondary austenite is found in locations of previous nitrides.

One general trend observed in all the experiments was that only one reheating cycle was enough to promote the formation of secondary austenite regardless of the time that the material was experiencing temperatures higher than 500 °C. What seems to be a key factor in the secondary austenite formation was the previous presence of nitrides in the ferrite matrix of the as-deposited pass and the number of reheating cycles experienced, which in turn was connected to the weld pass sequence layout (Figure 1), described in Section 3.5.

Regarding the σ-phase, in the FR weld, none of the weld passes experienced reheating in the critical temperature ranges, expect for Weld Pass 7, which was exposed for 5 s. However, some locations of the σ-phase were found in Weld Passes 1–6 (Figure 13).

In the GR weld, few locations with σ-phase were found in Weld Pass 1 (9 s reheated in the critical temperature range) and Weld Pass 4 (1 s reheated in the critical temperature range). As shown in Figure 1, Weld Pass 4 had four subsequent weld passes in the immediate vicinity.

In the GH weld, according to the thermal cycles, only Weld Pass 1 and Weld Pass 5 experienced some time (16 s and 3 s, respectively) in the critical temperature range for σ-phase formation. However, very small amounts of σ-phase were also found in Weld Pass 2 and Weld Pass 3, which never registered reheating in the critical temperature range.

As a whole, σ-phase was found in very small amounts (less than 1%) and always at δ/γ boundaries (Figure 13) in the three welds. As a general observation, it seems that the formation of σ-phase would involve at least three reheating cycles of the weld metal.

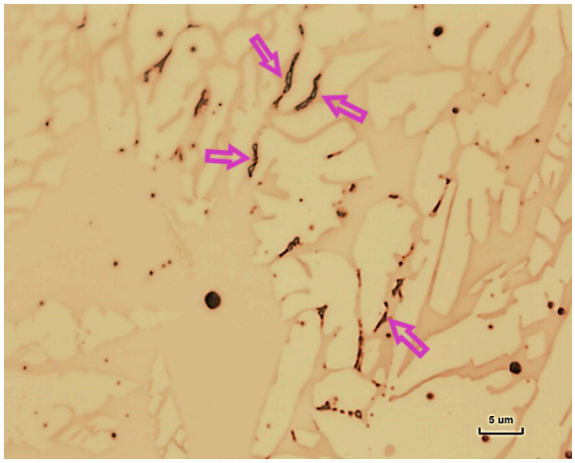

Figure 13. The σ-phase in Weld Pass 4, close to Weld Passes 5 and 6 in the FR weld.

In terms of the secondary phases, the microstructural evolution observed as a general trend in these experiments is illustrated in Figure 14, and it can be summarized as follows: the as-deposited material was free from nitrides or contained nitrides as previously discussed depending on the process, the arc energy, and consequently the cooling rate. After the first reheating, secondary austenite was observed in most cases in coexistence with nitrides. The σ-phase was observed when a pass had been reheated at least three times, and it was found in very small amounts (less than 1%) and always at δ/γ boundaries in the three welds.

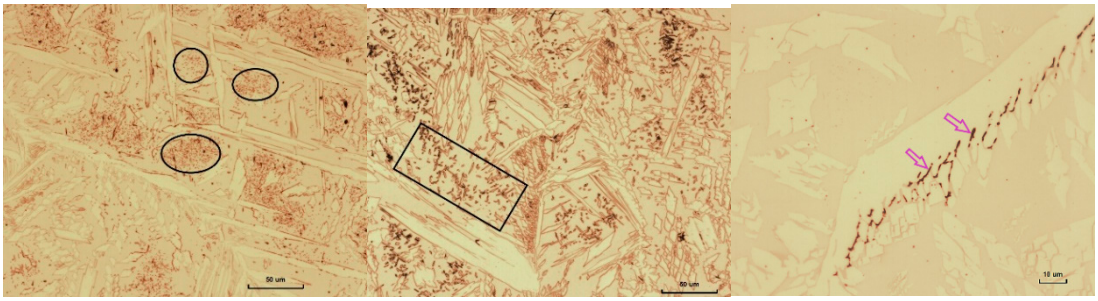

Figure 14. Micrographs from the GR welds showing the microstructure of Weld Pass 1 (GTAW Root). (**Left**) Massive amounts of nitrides in the ferrite grains in the as-deposited condition. (**Center**) Secondary austenite formation in the ferrite grains after reheated caused by Weld Pass 2. (**Right**) The σ-phase after six reheats.

3.5. The Welding Sequence Layout and the Thermal Cycles

The welding sequence layout (Figure 1) seems to play an important role in the distribution of secondary austenite and σ-phase. A larger amount and concentration of secondary austenite was found for a larger number of subsequent passes in the immediate vicinity of a specific weld pass. The same trend was seen for the preferred location for σ-phase formation. In the FR experiment, Weld Pass 7 was the only one with three weld passes in the immediate vicinity and it was the one experiencing the longest reheating time in the different critical temperature ranges studied: 20 s for γ_2 formation, 7 s for nitrides formation, and 5 s for σ-phase formation. Similarly, in the GR experiment, Weld Passes 4 and 6, both experiencing reheating caused by three subsequent weld passes showed the second longest reheating time in the critical ranges of temperatures: 23 s for γ_2 formation, 6 s for nitrides formation, and 6 s for σ-phase formation. In the GR experiment, the weld pass experiencing longer reheating times was the root pass: 40 s for γ_2 formation, 8 s for nitrides formation, and 9 s for σ-phase formation. In the GH experiment, the maximum number of subsequent neighboring passes was 2, and the root pass was by far the one experiencing the longest reheating time in the critical temperature ranges: 98 s for γ_2 formation, 13 s for nitride formation, and 16 s for σ-phase formation.

None of the weld passes in the experiments was at any time in the temperature ranges for the dissolution of σ-phase or nitrides, so dissolution of these phases was not expected.

When comparing the magnitude of the influence of the subsequent weld passes on one deposited pass, the time that the pass was exposed to higher than 500 °C was taken as a reference. The reason is that the formation of the intragranular secondary austenite (γ_2) was assumed to happen at temperatures higher than 500 °C [2,18], and as described in Section 2.4, it is the lowest temperature in the formation of the secondary phases considered. For the FR experiment, only the subsequent deposited passes in direct contact with the pass investigated had an influence (exposure time between 4 and 15 s to T > 500 °C). Interestingly, in the GR experiment, the two subsequent deposited passes had an influence (exposure times between 1 and 24 s to T > 500 °C) until Weld Pass 8, which was only influenced by Weld Pass 9 and not by Weld Pass 10 because of the welding layout (Figure 1). In the GR experiment, the root pass was influenced by the three subsequent deposited passes (exposure times between 26 and 44 s). These results were in agreement with the measured cooling rates (Figure 7): the slower

the cooling rate, the more time the pass was exposed to T > 500 °C, and more previously deposited passes were influenced.

3.6. Impact Toughness

Charpy-V impact toughness specimens were extracted from the center of the weld section aiming to assess both the absorbed energy in the weld metal and in the HAZ. The measurements obtained in both locations in the three welds exceeded the acceptance criteria 27 J of average absorbed energy at −46 °C with no single values below 70% of that average value according to Norsok M-601 [20]. Figure 15 summarizes the results and confirms that FR welds showed the lowest toughness, and GR showed the highest, with GH weld toughness in between. It is interesting to note that, in the FR weld, the toughness in the weld metal was lower than it was in the HAZ.

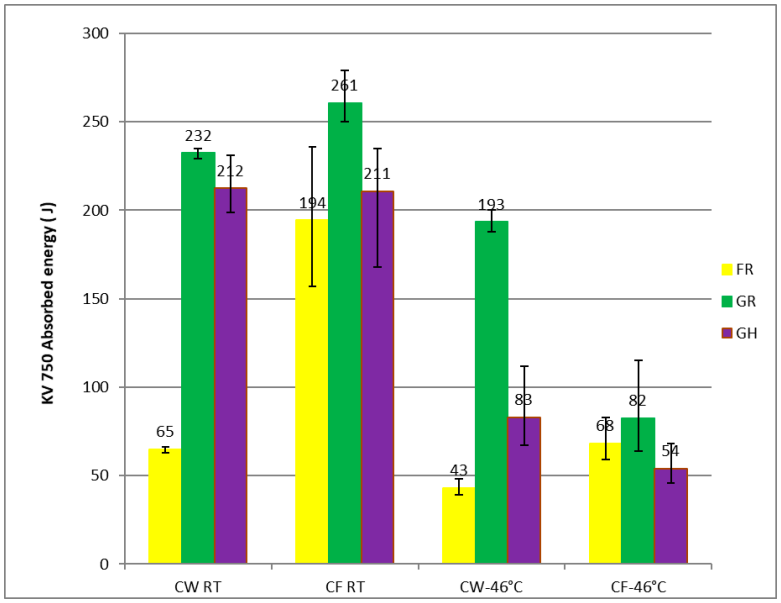

Figure 15. Charpy-V impact toughness results (CW: coupons extracted from the center of the weld section and with notch in the weld metal. CF: coupons extracted from the center of the weld section and with notch in the fusion line +2 mm). Tests performed at RT (room temperature) and at −46 °C.

As expected, the difference in the absorbed energies was in connection with the oxygen content measured in the welds (Figure 16) and consequently with the amount of micro-inclusions observed in the weld metal (Figure 17). There was a higher oxygen content, a higher amount of micro-inclusions in the FR weld, a lower oxygen content, and a practically unnoticeable amount of micro-inclusions in the GR weld.

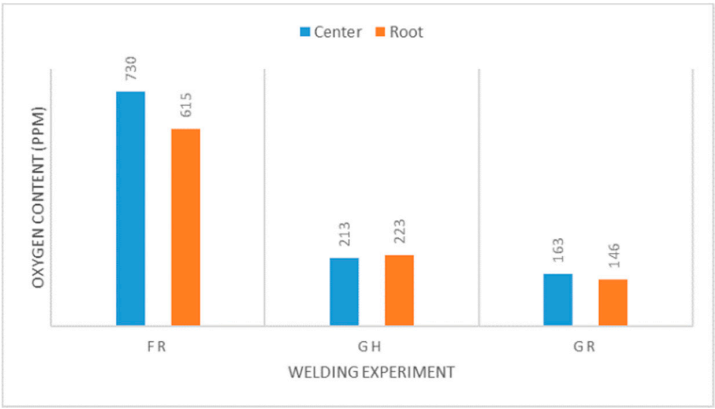

Figure 16. Oxygen content in the root and the center of the welds.

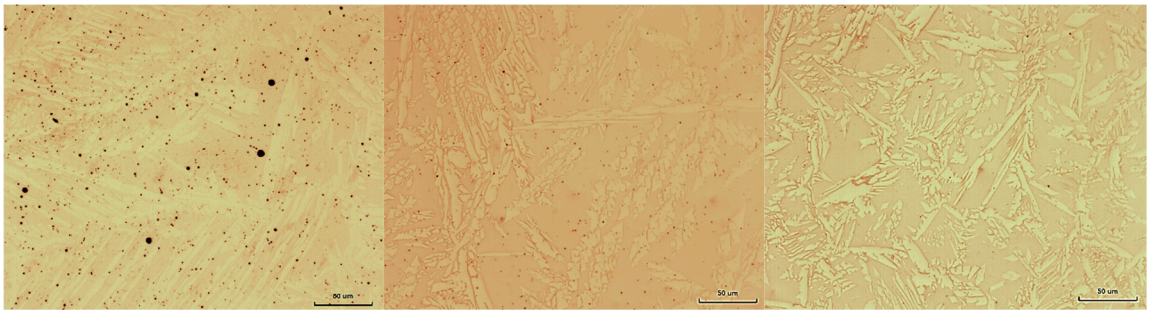

Figure 17. Micro-inclusions in the weld deposited metal (shown as black dots in the micrographs). (**Left**) FCAW experiment with recommended arc energy. (**Center**) GMAW experiment with higher-than-recommended arc energy. (**Right**) GMAW experiment with recommended arc energy.

3.7. Pitting Corrosion

The ASTM G48E corrosion test was used to evaluate the CPT in the three experiments. Both GMAW welds showed the same CPT of 55 °C, whilst the FCAW welds showed a lower CPT value of 50 °C. To rank the GMAW experiments with the same CPT, additional criteria were considered, such as the number and depth of the pits and the weight loss. The GR weld then showed a better ranking than the GH weld.

To compare the influence of the arc energy on the corrosion resistance of the GMAW welds, the ASTM G150 test was performed on GH and GR coupons. Table 3 summarizes the results from the ASTM G150 test together with relevant microstructural features and the location of the pitting initiation. Because of the differences in the time settings with the standard, the temperatures registered are not CPT strictly speaking, but they served comparison purposes.

Table 3. Results of ASTM G150 corrosion test, location of pitting initiation and microstructural features.

Experiment	Section Investigated and Microstructural Features Observed	CPT * (°C)	Location of Pitting Initiation
GR	Section investigated includes Weld Pass 2 and HAZ. The weld metal showed very few nitrides but the HAZ contained extensive amounts of nitrides	70.2	In the HAZ
GH	Section investigated includes weld passes 2 and 3 and HAZ. The weld metal showed χ_2 and σ-phase and the HAZ contained nitrides.	73.2	In the weld metal

* Not strictly critical pitting corrosion because of the differences in the time settings with the standard.

Porosity was not a concern in terms of pitting corrosion, as pores were surrounded by austenite (see Figure 18), most probably because of the presence of nitrogen in the pores.

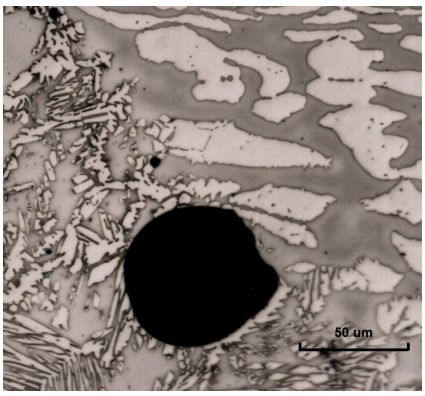

Figure 18. A pore (in black) surrounded in the majority of its perimeter by austenite phase (in white).

4. Discussion

4.1. Methodology

The methodology used to monitor the thermal cycles was found to be reliable and accurate. The combination of harpooned and inserted K-type thermocouples showed very low dispersion in the measurements, and more than 90% of thermocouples survived. To achieve these results, it was necessary to refine and optimize the methodology by comparing the performance of different thermocouple types (K, N, and C), by checking the influence of insulation material (Inconel® vs. glass-fiber) and by exploring different insertion and fitting techniques for the thermocouples [21,22]. As a result of that preliminary study, the methodology used in this work proved to be suitable and very convenient to study not only super-duplex multi-pass welds, but any kind of multi-pass-welded alloy in which the formation of deleterious phases could be a concern.

The experimental approach of shortening in length the weld passes in the joint configuration was found to be very useful to follow the evolution of the microstructure in the weld passes. This technique made it possible to obtain one coupon containing the as-deposited pass and the previous ones. Therefore, the microstructure of each single weld pass, in the as-deposited condition could be compared after each one of the reheats experienced.

4.2. Phases

4.2.1. Ferrite

The progressive increase of austenite in the weld metal caused by the reheating is reported in Section 3.3. The internal transformation into % ferrite in the feritscope can add some uncertainty to the measured values, but such values are still useful as an indication of the ferrite trend among the weld passes. New austenite is formed by the subsequent reheating: in the intragranular zones with the formation of secondary austenite and with the growth of the Widmanstätten laths and with the growth of the intergranular austenite. The higher arc energy and interpass temperature in the GH experiment resulted in a lower cooling rate in the weld metal and in a longer period for nitrogen and other elements to diffuse and form austenite, leading to the largest reduction in ferrite (12% ferrite decrease in Weld Pass 1). The presence of micro-inclusions in the GH weld could have additionally helped in the increase of austenite, as it is well known that inclusions act as potential nucleation sites for intragranular austenite.

4.2.2. Nitrides

As described in Section 3.4, the GH weld showed the lowest content of nitrides and no nitrides in some cases, despite having longer times at the critical temperature ranges; the GR weld showed the highest amount of nitrides and the FR weld was in between. These differences observed in terms of nitride content in the welds can be explained by the difference in cooling rates (Figure 7), influencing the nitrogen diffusion from ferrite to austenite. In addition, the level of micro-inclusions might play a role acting as nucleation sites for austenite and pinning the ferrite grain boundaries preventing grain growth, thus shortening the distance for nitrogen and other elements to diffuse.

To illustrate the importance of the latter phenomenon, in the GR weld, it was observed that the root pass (GTAW) contained significant amounts of nitrides after only 6 s in the critical temperature range, whilst the second weld pass (GMAW) did not present nitrides. The cooling rate (based on the cooling time $t_{12/8}$) of both passes was the same (38 °C/s). In this case, when cooling rates and therefore the time for nitrogen diffusion is the same, it is expected that larger ferrite grain sizes implies a longer distance for nitrogen to diffuse until reaching the austenite. Thus, precipitation of nitrides was found in the GTAW weld with a larger grain size. There was an absence of nitrides in the as-deposited GH welds, and there were very few nitrides in the reheated weld passes, despite having longer times in

the critical range compared with the other welds. This is explained by a low cooling rate (Figure 7), which allows more nitrogen diffusion to take place.

4.2.3. Secondary Austenite

Only one reheating cycle was needed to promote the formation of secondary austenite regardless of the time that the material was experiencing temperatures higher than 500 °C. Secondary austenite was found in former locations of nitrides (Figure 13). This observation supports the mechanism proposed by Ramirez et al. [23] relating the secondary austenite nucleation to former nitrides precipitation. The weld pass layout plays a role in the distribution of secondary austenite. The larger the number of passes in the immediate vicinity of the deposited metal, the larger the amount and concentration of secondary austenite. Therefore, in secondary austenite formation, the time during which the material is in the critical temperature range is less influential than the number of reheating cycles, as Hosseini et al. reported [24].

4.2.4. σ-Phase

As reported in Section 3.4, on some occasions, small amounts of σ-phase were found in weld passes that did not reach the critical temperature range (750 °C–1073 °C). In other cases, the time registered went from 1 s in GR to 16 s in GH, times that are on the lower end of times reported in the literature [25] or predicted by thermodynamics. JMatPro predicted for this experiment a TTT curve with a nose (990 °C, 34 s to have 1% σ-phase and 5 s to have 0.1% σ-phase)]. The reasons that might explain these current observations could be related to the following:

(a) Locations for thermal recording and for metallographic inspection are different. The coupons for metallographic inspection were extracted from close to the end point of the weld, i.e. close to the downslope, whilst the thermal recording was done at the start of the weld.
(b) It has been assumed that the temperatures registered locally and the cooling rates calculated are representative of the entire weld pass. However, in reality, there is a gradient in temperatures within the same weld pass, being the region close to the fusion boundary experiencing higher temperatures than the locations at a distance in the weld pass.
(c) The σ-phase could form randomly along the longitudinal weld direction due to local compositional segregation, and the specific section evaluated might contain or might not contain σ-phase.
(d) It might be that the kinetics to form σ-phase require longer times at lower temperatures than considered.

4.3. Properties

4.3.1. Toughness

All the welds met the impact toughness requirements, and not surprisingly the flux cored wire resulted in a weld metal with more micro-inclusions, a higher oxygen content, a lower impact toughness, and a lower CPT than the welds produced with solid wire, as reported in the literature for duplex stainless steels [26]

In terms of toughness in the HAZ, according to the results shown in Figure 14, absorbed energies in the HAZ showed lower dispersion than the absorbed energies in the weld metal. This means that there are no great differences among the HAZs in the experiments. For the experiment FR, at each testing temperature, toughness in the WM was lower than in the HAZ. Therefore, inclusions and σ-phase found in the WM were more detrimental than nitrides in the HAZ.

4.3.2. Pitting Corrosion

It is well-known that nitrides and σ-phase decrease pitting resistance because of the adjacent depletion in Cr and N (in the case of nitrides) and in Mo (in the case of σ-phase) [27–30]. It is also recognised that γ_2 has lower amounts of N, Cr, and Mo compared to intergranular γ and Widmanstätten γ [25,31], which is also detrimental for corrosion resistance. When the weld metal was free from the above-mentioned secondary phases, as in the GR weld coupon, the HAZ that always contained nitrides became the weakest location for pitting initiation.

4.4. Implications on Practical Welding

The results of this work have some implications on practical welding. Until now, the welding guidelines [9–11] were clear in limiting the maximum arc energy used to 1.5 kJ/mm. However, in the case of large thickness weldments such as the 20 mm studied here, the use of 2.0–2.2 kJ/mm was not found to be detrimental. The number of weld passes was reduced from 10 to 7, which implies a lower number of reheating cycles for the deposited passes and therefore less secondary austenite formation. In addition, the weld with higher-than-recommended arc energy (GH) showed no nitrides in the as-deposited weld and fewer nitrides in the overall weld. The CPT values for both GMAW welds (GR and GH) were found to be the same, and the results of the toughness test exceeded the acceptance criteria. These findings promote the use of a higher-than-recommended arc energy in large thickness weldments of super-duplex stainless steels.

Based on the results from this work, the welding sequence layout should be considered when welding superduplex stainless steels. To have weld passes surrounded by three or more subsequent weld passes should be avoided, as this would result in larger amounts of secondary austenite and σ-phase.

5. Conclusions

- Multi-pass 20 mm welds of superduplex plates were produced with GMAW and FCAW with recommended and higher arc energies accomplishing the impact toughness requirements.
- A new methodology for monitoring the thermal cycles and the microstructural evolution was shown to be successful and was consolidated.
- Reheating by subsequent passes caused a progressive increase in the austenite content of the weld metal.
- The cooling rate and not the time exposed at the critical temperature range is the key factor in the nitrides formation. However, when cooling rates are the same, larger ferrite grains enhanced the precipitation of nitrides, as it implied a longer distance for nitrogen to diffuse until reaching the austenite phase.
- A larger amount and concentration of secondary austenite and σ-phase was found for a larger number of subsequent passes in the immediate vicinity of a specific weld pass.
- Pitting corrosion preferentially initiated in locations with secondary austenite and σ-phase. However, when the weld metal was free from these secondary phases, the nitrides in the HAZ were the weakest location where pitting initiated.
- The results of this work have implications on practical welding for superduplex stainless steels: from the microstructural point of view, the current recommendations on maximum arc energy should be revised for large thickness weldments and the importance, of the welding sequence on the formation of secondary phases should be considered.

Author Contributions: Conceptualization: M.A.V.B. and L.K.; Funding acquisition: M.A.V.B. and L.K.; Investigation: M.A.V.B., K.H., and D.E.; Methodology: K.H. and L.K.; Project administration: M.A.V.B.; Supervision: L.K.; Validation: K.H. and D.E.; Visualization: M.A.V.B.; Writing—original draft: M.A.V.B.; Writing—review & editing: L.K.

Funding: This research was funded by KK-stiftelsen (Stiftelsen för kunskaps- och kompetensutveckling), grant number 20140046.

Acknowledgments: Cecilia Lille (Outokumpu Stainless AB), Hans Åstrom (Elga AB), Per Bengtsson (AGA Gas AB), and Matti Karvinen (Howden Turbo Fans Oy) are gratefully acknowledged. The cooperation from Elisabeth Johansson and Jan Björk from the corrosion lab at Avesta R&D Center is sincerely acknowledged. Huge thanks to colleagues Vahid A. Hosseini, Kenneth Andersson, and Mattias Ottosson at University West for their support in this project.

Conflicts of Interest: The authors declare no conflict of interest. The funders had no role in the design of the study; in the collection, analyses, or interpretation of data; in the writing of the manuscript; or in the decision to publish the results.

References

1. Charles, J. Duplex stainless steels, a review after DSS'07 held in Grado. In Proceedings of the Duplex Stainless Steel Conference, Maastricht, The Netherlands, 18–20 June 2007.
2. Karlsson, L. Intermetallic Phase Precipitation in Duplex Stainless Steels and Weld Metals Metallurgy, Influence on Properties and Welding Aspects. *Weld. World* **1999**, *43*, 20–41.
3. Karlsson, L.; Rigdal, S.; Pak, S. Effects of elemental distribution on precipitation behaviour and properties of duplex stainless steel weldments. In Proceedings of the Duplex Stainless Steel Conference, Venice, Italy, 17–20 October 2000.
4. Valiente Bermejo, M.A.; Karlsson, L.; DebRoy, T. Influence of low energy laser welding on solidification and microstructure of austenitic stainless steel welds. In Proceedings of the NOLAMP-14 Conference, Göteborg, Sweden, 26–28 August 2013; pp. 3–14.
5. Valiente Bermejo, M.A.; DebRoy, T.; Hurtig, K.; Karlsson, L.; Svensson, L.-E. Towards a map of solidification cracking risk in laser welding of austenitic stainless steels. *Phys. Procedia* **2015**, *78*, 230–239. [CrossRef]
6. Hosseini, V.A.; Valiente Bermejo, M.A.; Gårdstam, J.; Hurtig, K.; Karlsson, L. Influence of multiple thermal cycles on microstructure of heat-affected zone in TIG-welded super duplex stainless steel. *Weld. World* **2016**, *60*, 233–245. [CrossRef]
7. Hosseini, V.A.; Wessman, S.; Hurtig, K.; Karlsson, L. Nitrogen loss and effects on microstructure in multipass TIG welding of a super duplex stainless steel. *Mater. Des.* **2016**, *98*, 88–97. [CrossRef]
8. Segerstark, A.; Andersson, J.; Svensson, L.-E. Evaluation of a temperature measurement method developed for laser metal deposition. *Sci. Technol. Weld. Join.* **2016**, *22*, 1–6. [CrossRef]
9. *How to Weld Duplex Stainless Steels*; Document 10601EN-GB; Avesta Welding AB: Avesta, Sweden, 2006; 20p.
10. *Welding Guidelines for Duplex & Superduplex Stainless Steels*; Metrode Products Ltd.: Chertsey, UK, 2005; 7p.
11. Pettersson, C.-O.; Fager, S.-Å. *Welding Practice for the Sandvik Duplex Stainless Steels SAF 2304, SAF 2205 and SAF 2507*; Technical Document S-91-57; AB Sandvik Steel: Stockholm, Sweden, 1995; 15p.
12. Valiente Bermejo, M.A.; Karlsson, L.; Svensson, L.-E.; Hurtig, K.; Rasmuson, H.; Frodigh, M.; Bengtsson, P. Effect of shielding gas on welding performance and properties of duplex and superduplex stainless steel welds. *Weld. World* **2015**, *59*, 239–249. [CrossRef]
13. Valiente Bermejo, M.A.; Karlsson, L.; Svensson, L.-E.; Hurtig, K.; Rasmuson, H.; Frodigh, M.; Bengtsson, P. Effect of welding position on properties of duplex and superduplex stainless steel circumferential welds. *Weld. World* **2015**, *59*, 693–703. [CrossRef]
14. Stützer, J.; Zinke, M.; Jüttner, S. Studies on the pore formation in super duplex stainless steel welds. *Weld. World* **2017**, *61*, 351–359. [CrossRef]
15. Swedish Standards Institute. *ISO 9016:2012. Destructive Tests on Welds in Metallic Materials—Impact Test—Test Specimen Location, Notch Orientation and Examination*; Swedish Standards Institute: Stockholm, Sweden; 20p.
16. ASTM International G48. *Standard Test Methods for Pitting and Crevice Corrosion Resistance of Stainless Steels and Related Alloys by Use of Ferric Chloride Solution*; ASTM International: West Conshohocken, PA, USA, 2011; 11p.
17. ASTM International G150-99. *Standard Test Method for Electrochemical Critical Pitting Temperature Testing of Stainless Steels*; ASTM International: West Conshohocken, PA, USA, 2004; 13p.
18. Nilsson, J.-O.; Chai, G. The physical metallurgy of DSS. In Proceedings of the Duplex Stainless Steel Conference, Beaune, France, 13–15 October 2010; pp. 369–390.

19. Pettersson, N.; Wessman, S.; Hertzman, S.; Studer, A. High-Temperature Phase Equilibria of Duplex Stainless Steels Assessed with a Novel In-Situ Neutron Scattering Approach. *Metall. Mater. Trans.* **2017**, *48*, 1562–1571. [CrossRef]
20. Standards Norway. NORSOK Standard M-601. Rev. 4, Welding and inspection of piping. 2004; 20p.
21. Valiente Bermejo, M.A.; Hurtig, K.; Hosseini, V.A.; Karlsson, L.; Svensson, L.-E. Monitoring thermal cycles in multi-pass welding. In Proceedings of the 7th International Swedish Production Symposium (SPS-16), Lund, Sweden, 25–27 October 2016.
22. Valiente Bermejo, M.A.; Hurtig, K.; Karlsson, L.; Svensson, L.-E. A step forward in understanding superduplex multi-pass welds by monitoring thermal cycles. In Proceedings of the 70th IIW Annual Assembly, Shanghai, China, 28 June 2017.
23. Ramirez, A.J.; Brandi, S.D.; Lippold, J.C. Secondary austenite and chromium nitride precipitation in simulated heat affected zones of duplex stainless steels. *Sci. Technol. Weld. Join.* **2013**, *9*, 301–313. [CrossRef]
24. Hosseini, V.A. Influence of Multiple Welding Cycles on Microstructure and Corrosion Resistance of a Super Duplex Stainless Steel. Licentiate Thesis, University West, Trollhättan, Sweden, 2016.
25. Hosseini, V.A.; Karlsson, L.; Engelberg, D.; Wessman, S. Time-temperature-precipitation and property diagrams for super duplex stainless steel weld metals. *Weld. World* **2018**, *62*, 517–533. [CrossRef]
26. Zhang, Z.; Jing, H.; Xu, L.; Han, Y.; Zhao, L. Investigation on microstructure evolution and properties of duplex stainless steel joint multi-pass welded by using different methods. *Mater. Des.* **2016**, *109*, 670–685. [CrossRef]
27. Hosseini, V.A.; Hurtig, K.; Karlsson, L. Effect of multipass TIG welding on the corrosion resistance and microstructure of a super duplex stainless steel. *Mater. Corros.* **2017**, *68*, 405–415. [CrossRef]
28. Hosseini, V.; Karlsson, L.; Wessman, S.; Fuertes, N. Effect of sigma phase morphology on the degradation of properties in a super duplex stainless steel. *Materials* **2018**, *11*, 933. [CrossRef] [PubMed]
29. Yousefieh, M.; Shamanian, M.; Saatchi, A. Influence of step annealing temperature on the microstructure and pitting corrosion resistance of SDSS UNS S32760 welds. *J. Mater. Eng. Perform.* **2011**, *20*, 1678–1683. [CrossRef]
30. Kobayashi, D.Y.; Wolynec, S. Evaluation of the low corrosion resistant phase formed during the sigma phase precipitation in duplex stainless steels. *Mater. Res.* **1999**, *2*, 239–247. [CrossRef]
31. Nilsson, J.-O.; Karlsson, L.; Andersson, J.-O. Secondary austenite formation and its relation to pitting corrosion in duplex stainless steel weld metal. *Mater. Sci. Technol.* **1995**, *11*, 276–283. [CrossRef]